buildings

MDPI

Article

Durability Performance and Microstructural Evolution of Carbonation-Solidified Red Mud-Based Backfill Under Wetting–Drying Cycles and Alkaline Red Mud Liquor Immersion

Lizhu Qi [1], Tanjia Zhang [1], Dechao Cui [1], Shiqi Chang [2], Xiaoqiang Dong [1,3,*] and Junlian Yin [4]

[1] College of Civil Engineering, Taiyuan University of Technology, Taiyuan 030024, China; qlzsxcig@163.com (L.Q.); zhangtanjia0145@link.tyut.edu.cn (T.Z.); cuidechao9022@link.tyut.edu.cn (D.C.)
[2] College of Engineering Management, Shanxi Vocational University of Engineering Science and Technology, Jinzhong 030619, China; changshiqi@sxgkd.edu.cn
[3] College of Applied Science, Taiyuan University of Science and Technology, Taiyuan 030024, China
[4] Coal Industry Taiyuan Design and Research Institute Group Co., Ltd., Taiyuan 030024, China; yjl4116796@163.com
* Correspondence: dongxiaoqiang@tyut.edu.cn

Abstract

Red mud-based backfill containing circulating fluidized bed (CFB) ash and reactive MgO must maintain adequate mechanical integrity and environmental stability under moisture and alkaline exposure. This study investigated the durability of carbonation-solidified red mud-based backfill subjected to wetting–drying cycles and alkaline red mud liquor (RML) immersion. Specimens carbonated for 0, 2, 4, 6, 8, and 10 h were evaluated in terms of macroscopic morphology, mass loss, linear shrinkage, unconfined compressive strength (UCS), electrical resistivity, pH, hazardous-element leaching, scanning electron microscopy, and X-ray diffraction. Increasing carbonation duration generally reduced mass loss and linear shrinkage while improving UCS and electrical resistivity within the investigated exposure range. Wetting–drying cycling resulted in progressive surface erosion, shrinkage, and strength deterioration. By contrast, RML immersion produced an initial increase in UCS and resistivity, followed by stabilization or a slight decline at later ages. The observed changes were consistent with pore filling by carbonate-bearing products and low-crystallinity reaction products, followed by local pore development and disruption of the cemented structure during prolonged exposure. At a UCS threshold of 0.8 MPa, the response-surface models yielded estimated threshold exposures of 6.92–13.98 cycles under wetting–drying conditions and 45.69–75.05 d under RML immersion, with the RML estimates extrapolated from the 28 d dataset. Within the tested conditions, carbonation improved the resistance of the backfill material to cyclic moisture disturbance and alkaline immersion, with the 8–10 h groups retaining relatively higher mechanical and dimensional performance.

Keywords: red mud; carbonation curing; MgO; CFB ash; backfill material; wetting–drying cycle; alkaline erosion; unconfined compressive strength; electrical resistivity; service-life prediction

Check for updates

Academic Editor: Shengwen Tang

Received: 23 June 2026
Revised: 30 July 2026
Accepted: 4 August 2026
Published: 6 August 2026

Copyright: © 2026 by the authors. Licensee MDPI, Basel, Switzerland. This article is an open access article distributed under the terms and conditions of the Creative Commons Attribution (CC BY) license.

1. Introduction

Red mud is an alkaline industrial residue generated during alumina production. Its high alkalinity, fine particle size and potential trace-element mobility restrict direct reuse,

while long-term stockpiling occupies land and creates environmental pressure [1,2]. Converting red mud into cemented or solidified backfill material is therefore attractive, because it can consume large quantities of residue and simultaneously provide a load-bearing geomaterial for mining or civil engineering applications [3–5].

The engineering feasibility of red mud-based backfill depends not only on initial strength, but also on durability under coupled mechanical, hydraulic and chemical actions [6]. In field conditions, backfill materials may experience repeated wetting and drying, alkaline seepage, pore-solution migration and local crystallization [7]. These processes can alter pore connectivity, weaken cementation products and accelerate the development of microcracks [8]. A reliable durability assessment should therefore combine macroscopic damage indicators, mechanical performance, electrical response, environmental leaching and microstructural evidence [9–11].

MgO-assisted carbonation offers a promising pathway for solidifying alkaline wastes. During curing, MgO hydrates to $Mg(OH)_2$ and then reacts with CO_2 to form magnesium carbonate phases [12,13]. Meanwhile, the alkaline environment can activate Si- and Al-bearing components in CFB ash and red mud, generating low-crystallinity gels such as M-S-H, M-A-S-H, C-A-S-H and N-A-S-H. Carbonate crystals and gel products may jointly fill pores, bind particles and immobilize potentially hazardous elements [14]. However, the extent to which this composite cementation structure resists wetting–drying damage and alkaline red mud liquor immersion remains insufficiently quantified [15,16].

Previous studies have clarified the strength development and phase evolution of reactive-MgO materials under carbonation and have examined red mud and CFB ash as constituents of cementitious or backfill systems [17–23]. However, the durability response of a red mud–CFB ash–MgO backfill under combined carbonation and subsequent environmental exposure remains insufficiently understood. In particular, the influence of carbonation duration on deterioration under cyclic wetting–drying and continuous alkaline red mud liquor immersion has not been evaluated within a unified experimental framework. The relationships among mechanical retention, electrical response, chemical evolution, and microstructural change also require further clarification [24–27].

To address these issues, six carbonation durations of 0, 2, 4, 6, 8, and 10 h were investigated. Durability was evaluated at 2, 6, and 10 wetting–drying cycles and at RML immersion ages of 0, 3, 7, 14, and 28 d using macroscopic morphology, mass loss, linear shrinkage, unconfined compressive strength, electrical resistivity, pH, hazardous-element leaching, SEM, and XRD. The study aimed to quantify the effect of carbonation duration on performance retention, compare the responses induced by cyclic moisture variation and continuous alkaline immersion, examine the relationship between UCS and electrical resistivity, and establish strength-response models for the two exposure regimes. The SEM and XRD results were further used to relate the measured macroscopic changes to the corresponding microstructural and phase evolution.

2. Materials and Methods

2.1. Materials and Specimen Preparation

2.1.1. Raw Materials

The red mud and circulating fluidized bed (CFB) ash used in this study were obtained from Xiaoyi, Shanxi Province, China. The red mud was generated from the Bayer alumina-production process, whereas the CFB ash was collected from a local circulating fluidized bed power plant. Commercial reactive MgO supplied by Hefei Meishen Technology Co., Ltd. (Hefei, China) was used as the Mg-bearing binder. The MgO was obtained from a single production batch and contained 95.30 wt.% MgO. A polycarboxylate superplasticizer was incorporated to maintain the flowability and homogeneity of the fresh slurry.

The chemical compositions of the red mud, reactive MgO, and CFB ash were determined by X-ray fluorescence spectroscopy and are listed in Table 1. The red mud was characterized by relatively high contents of Al_2O_3, SiO_2, CaO, Fe_2O_3, and Na_2O, whereas the CFB ash was dominated by SiO_2 and Al_2O_3. Particle-size analysis showed unimodal distributions for both solid wastes, with modal particle sizes of 23.96 μm for red mud and 37.47 μm for CFB ash. The raw powders were used in their received condition without grinding or chemical pretreatment.

Table 1. Chemical compositions of the raw materials determined by XRF (wt.%).

Material	CaO	SiO_2	Al_2O_3	Fe_2O_3	K_2O	MgO	Na_2O	SO_3	Other
Red mud	18.26	20.17	24.34	9.40	0.64	1.26	9.61	0.19	16.13
Reactive MgO	0.55	1.12	0.65	0.12	0.00	95.30	0.00	0.11	2.15
CFB ash	4.40	57.30	22.60	5.80	2.00	4.70	1.34	0.60	1.26

2.1.2. Mixture Proportion and Specimen Preparation

The durability experiments were conducted using the M2 mixture, which exhibited comparatively stable mechanical and electrical performance in the preliminary mixture-screening tests. The red mud content was taken as 100 parts by mass, with reactive MgO, CFB ash, and polycarboxylate superplasticizer added at 12.5, 2.5, and 2.3 parts, respectively. Accordingly, the mass ratio of CFB ash to reactive MgO was 1:5. The superplasticizer dosage corresponded to 2.0 wt.% of the total solid constituents, and the water-to-solid ratio was fixed at 0.50. This mixture was used for all durability specimens so that carbonation duration remained the only varied preparation parameter.

Red mud, reactive MgO, and CFB ash were dry-mixed for 10 min to obtain a uniform solid blend. The polycarboxylate superplasticizer was dissolved in the prescribed amount of water before being added gradually to the dry mixture. The resulting slurry was mixed at 100 r/min until no visible agglomeration remained. It was then placed in several increments into cylindrical moulds with an internal diameter of 50 mm and a height of 50 mm. The specimen geometry was selected during the preliminary experimental programme so that the same cylindrical configuration could be used for mass, dimensional, electrical-resistivity, and mechanical measurements. A constant diameter of 50 mm and height of 50 mm were maintained for all carbonation durations and exposure conditions, thereby avoiding specimen-size variation within the present comparative study. The inner surfaces of the moulds were coated with silicone oil to facilitate demoulding. Low-frequency vibration was applied after each filling step until visible air bubbles ceased. No external static compaction pressure was applied. The upper surfaces were levelled, and the moulds were covered with plastic film to restrict moisture loss during pre-curing.

2.1.3. Carbonation and Subsequent Curing

After casting, the specimens were covered and pre-cured for 18 h at 20 ± 2 °C and 75 ± 2% relative humidity. They were subsequently demoulded and assigned to carbonation durations of 0, 2, 4, 6, 8, and 10 h. Carbonation was conducted in a sealed pressure-controlled vessel at 60 °C, 80% relative humidity, a CO_2 concentration of 80 vol.%, and a total gas pressure of 0.2 MPa. Internal gas circulation was maintained throughout the carbonation period to homogenize the chamber atmosphere. As the vessel operated as a closed pressure-controlled system, no external continuous gas flow was supplied during carbonation. The 0 h specimens underwent the same preparation and curing procedures without exposure to the pressurized CO_2 atmosphere.

After carbonation, all specimens were transferred to a controlled curing room maintained at 20 ± 2 °C and 75 ± 2% relative humidity. They were cured to a total age of 28 d

before being subjected to the wetting–drying and red mud liquor immersion tests. The mixture composition, specimen geometry, pre-curing conditions, and subsequent curing age were kept constant, with carbonation duration as the only preparation variable.

2.2. Durability Exposure Regimes

Two exposure regimes were applied to the specimens after curing to 28 d: wetting–drying cycling in deionized water and continuous immersion in Bayer-process red mud liquor. The procedures for the two regimes are described below.

2.2.1. Wetting–Drying Cycles

The wetting–drying test was conducted using deionized water as the immersion medium. During the wetting stage, the specimens were completely immersed at 20 ± 2 °C for 24 h, with the water level maintained at least 20 mm above the upper surface of the specimens. Fresh deionized water was used at the beginning of each cycle. After immersion, the specimens were removed from the containers, and surface water was gently blotted with absorbent paper. They were subsequently dried in a ventilated oven at 60 °C for 24 h. One 24 h immersion stage followed by one 24 h drying stage constituted a complete wetting–drying cycle.

After oven drying and cooling to room temperature, the mass and dimensions of the specimens were measured. Quantitative measurements of mass loss, linear shrinkage, UCS, electrical resistivity, and pH were conducted after 0, 2, 4, 6, 8, and 10 cycles. Macroscopic morphology was recorded after 2, 6, and 10 cycles. Separate specimens assigned to the corresponding exposure levels were used for destructive UCS and microstructural measurements.

2.2.2. Red Mud Liquor Immersion

Fresh red mud liquor generated during the Bayer alumina-production process was collected from the same production source in Xiaoyi, Shanxi Province, China. The liquor was used in its original condition without dilution or chemical adjustment. Specimens cured to 28 d were placed individually in polyethylene containers and completely immersed in the liquor. The liquid level was maintained at least 20 mm above the upper surface of each specimen throughout the exposure period. This immersion geometry was adopted to maintain unrestricted contact between the intact specimen and the exposure medium.

Because intact cylindrical specimens rather than crushed powders were exposed, the immersion condition was defined by complete submergence and a constant liquid cover depth instead of the powder-based liquid-to-solid ratio commonly used in batch extraction tests. The red mud liquor was a source-derived process solution rather than a synthetically prepared medium; therefore, no nominal ionic composition was imposed or adjusted during the exposure test. The initial pH of each fresh liquor batch was measured before use and remained within the range recorded for the original production liquor.

The containers were stored at 20 ± 2 °C, and the red mud liquor was completely replaced every 7 d to limit changes in alkalinity and dissolved-ion composition during prolonged exposure. The selected immersion ages were 0, 3, 7, 14, and 28 d. At each testing age, the specimens were removed from the liquor, rapidly rinsed with deionized water to remove residual surface deposits, and gently blotted with filter paper before mass, dimensional, UCS, electrical resistivity, and pH measurements. Macroscopic morphology was also documented at each exposure age.

2.3. Characterization Methods

The durability response was evaluated using a multi-index framework. Surface morphology was recorded to identify visible erosion, particle shedding, edge damage and

salt deposition. Mass variation and linear shrinkage were used to quantify material loss and deformation. UCS was measured to evaluate load-bearing capacity, whereas electrical resistivity was used as a non-destructive indicator of pore connectivity and internal structural integrity. pH measurements were conducted to track the evolution of alkalinity. Hazardous-element leaching was assessed for Na, As, Hg, Cd, Pb and Cu to evaluate environmental safety. SEM and XRD were used to examine microstructural evolution and phase assemblage.

For mass loss, the mass loss ratio was calculated from the initial mass and the mass after exposure [28]:

$$m_R = \frac{m_0 - m_t}{m_0} \times 100\% \quad (1)$$

where M_R is the mass loss ratio, m_0 is the initial specimen mass and m_t is the mass after the specified exposure time or cycle number.

For each carbonation duration and exposure condition, three parallel cylindrical specimens were used for the quantitative measurements. Unless otherwise stated, the results are expressed as mean ± standard deviation (n = 3), and the coefficient of variation is reported to describe the dispersion among parallel specimens. Mass, height, electrical resistivity, and pH were measured before UCS testing, while separate specimen sets were assigned to each exposure interval because UCS testing was destructive. SEM and XRD analyses were conducted on representative specimens selected from the corresponding exposure groups. For SEM, the 4 h and 8 h carbonation groups represented intermediate and longer carbonation conditions, while 2 and 8 wetting–drying cycles and 3 and 28 d of RML immersion represented early and later exposure states. For wetting–drying XRD, the 2 h and 8 h groups were selected to contrast short and longer carbonation. For RML XRD, the 10 h group at 7, 14, and 28 d was selected to isolate phase evolution with immersion time under a consistently well-carbonated condition. The microstructural programme was intended to interpret the principal performance contrasts rather than provide a complete factorial phase and morphology dataset.

The complete numerical datasets are provided in Supplementary Tables S1–S5. For each quantitative condition, the tables report the mean value, standard deviation, and coefficient of variation. Percentage differences relative to the non-carbonated group were calculated using the unrounded mean values at the same exposure level. Where applicable, the retention or change relative to the corresponding pre-exposure value was also reported. Positive and negative percentage values indicate increases and decreases, respectively.

Unconfined compressive strength was determined using cylindrical specimens 50 mm in diameter and 50 mm in height, corresponding to a height-to-diameter ratio of 1.0. Before testing, the loading surfaces were levelled and cleaned to remove loose particles and ensure uniform contact with the loading platens. All specimens entered the durability exposure programme at a curing age of 28 d. UCS tests were conducted after 0, 2, 4, 6, 8, and 10 wetting–drying cycles or after 0, 3, 7, 14, and 28 d of RML immersion. A YHS-229WJ-50 kN computer-controlled universal testing machine was used in accordance with JTG E51-2009. Axial displacement was applied at a constant rate of 1.5 mm/min until peak load and specimen failure. UCS was calculated by dividing the peak axial load by the initial cross-sectional area. Three parallel specimens were tested for each carbonation duration and exposure condition, and the observed failure patterns were recorded as axial splitting, inclined shear, or mixed splitting–shear failure.

Electrical impedance was measured using a two-electrode method with a TH2828A LCR digital bridge. Two parallel stainless-steel plate electrodes were placed in direct contact with the circular end surfaces of each specimen. Before measurement, the specimen ends and electrode surfaces were cleaned to remove loose particles. A constant contact pressure

of 7.5 kPa was applied without conductive paste. Alternating-current impedance was recorded over a frequency range of 50 Hz to 1 MHz, and the value obtained at 1 kHz was used for comparative analysis.

Electrical resistivity was determined from the measured impedance, specimen cross-sectional area, and electrode spacing:

$$\rho = \frac{|Z|A}{L} \tag{2}$$

where ρ is the electrical resistivity, $|Z|$ is the impedance magnitude measured at 1 kHz, A is the cross-sectional area of the specimen, and L is the distance between the two electrodes.

Specimens subjected to wetting–drying cycling were measured after the prescribed 60 °C drying stage and cooling to 20 ± 2 °C. Specimens subjected to RML immersion were rinsed with deionized water, blotted to remove visible surface liquid, and measured at 20 ± 2 °C. The conditioning and contact procedures were kept consistent within each exposure regime.

The pH values were determined from powder–water suspensions rather than from the external exposure solution or specimen surface. For each condition, 100 g of material passing a 5 mm sieve was mixed with 1 L of distilled water and shaken horizontally at 110 cycles/min for 8 h. The suspension was then allowed to stand for 16 h and filtered before measurement using a calibrated pH meter in accordance with GB 5085.3-2007. Three independent extracts were prepared and measured for each exposure condition.

Hazardous-element leaching was conducted in accordance with HJ/T 299-2007, Solid Waste–Extraction Procedure for Leaching Toxicity–Sulphuric Acid and Nitric Acid Method. Approximately 150 g of crushed material passing a 9.5 mm sieve was used for each extraction. The extraction fluid was prepared by adjusting distilled water to pH 3.20 ± 0.05 with a concentrated H_2SO_4–HNO_3 mixture at a mass ratio of 2:1, and a liquid-to-solid ratio of 10 L/kg was adopted. The sealed vessels were rotated at 30 r/min for 18 ± 2 h at 23 ± 2 °C. The extracts were filtered and analysed for Na, As, Hg, Cd, Pb, and Cu by ICP–OES. Three independent extracts were analysed for each reported condition. Method blanks were included in each analytical batch, and element-specific detection limits and spike-recovery results are reported in the note to the corresponding tables. Concentrations below the method detection limit are expressed as <LOD.

2.4. Strength Coupling and Service-Life Prediction

To describe the coupling between carbonation enhancement and durability damage, strength evolution was decomposed into strengthening and degradation terms. For wetting–drying conditions [29–31], the UCS can be expressed as the difference between the carbonation-enhanced initial strength and the wetting–drying-induced strength loss:

$$q_u(N, t_c) = q_u^0(t_c) - \Delta q_u(N, t_c) \tag{3}$$

$$q_u^0(t_c) = q_{ur} + q_{uc}(1 - e^{(-\alpha t_c)}) \tag{4}$$

$$\Delta q_u(N, t_c) = \delta N^m e^{(-\gamma t_c)} \tag{5}$$

$$q_u(N, t_c) = q_u r + q_u c(1 - e^{(-\alpha t_c)}) - \delta N^m e^{(-\gamma t_c)} \tag{6}$$

where q_u is UCS, N is the number of wetting–drying cycles, t_c is carbonation time, $q_{u,r}$ is the reference strength without carbonation, $q_{u,c}$ is the maximum carbonation-induced strength increment, α is the carbonation enhancement rate coefficient, λ is the damage coefficient, m is the damage development exponent, and γ is the durability improvement coefficient associated with carbonation [32].

For RML immersion, the strength evolution was described by considering carbonation enhancement, early alkaline activation and long-term erosion damage:

$$q_u(T_a,\ t_c) = q_u^0(t_c) + \Delta q_a(T_a) - \Delta q_e(T_a,\ t_c) \tag{7}$$

$$q_u^0(t_c) = q_{u,c} + q_{u,c}[1 - exp(-\alpha t_c)] \tag{8}$$

$$\Delta q_a(T_a) = \eta[1 - exp(-kT_a)] \tag{9}$$

$$\Delta q_e(T_a,\ t_c) = \mu T_a^n exp(-\gamma t_c) \tag{10}$$

$$q_u(T_a,\ t_c) = q_{u,c} + q_{u,c}[1 - exp(-\alpha t_c)] + \eta[1 - exp(-kT_a)] - \mu T_a^n exp(-\gamma t_c) \tag{11}$$

where T_a is the RML immersion time, η and κ describe the early alkaline activation effect, μ and n describe erosion damage, and the remaining parameters have the same physical meaning as above.

The coupled strength functions were used to describe the measured UCS evolution with carbonation duration and exposure level. The model separates the carbonation-related increase in initial strength from the subsequent exposure-related change in strength. For wetting–drying exposure, the deterioration term increases with cycle number and is moderated by carbonation, whereas the RML function describes the early strength increase followed by stabilization or gradual deterioration. The fitted parameters provide a compact description of the observed responses and are not interpreted as independently measured material constants.

For strength-threshold estimation, second-order response surfaces were subsequently fitted to the UCS datasets. At each carbonation duration, the threshold exposure level was obtained by setting the predicted UCS equal to q_{cr} = 0.8 MPa and solving for the corresponding number of wetting–drying cycles or RML immersion time.

3. Results

3.1. Surface Morphology Evolution

3.1.1. Wetting–Drying Cycles

The surface morphology of specimens subjected to wetting–drying cycles is shown in Figure 1. In the specimen labels, the value followed by "h" denotes the carbonation duration, whereas N denotes the number of wetting–drying cycles. For example, "8h-N=6" represents a specimen carbonated for 8 h and subsequently subjected to six wetting–drying cycles. Both cycle number and carbonation time affected the visible integrity of the specimens. As the number of cycles increased from 2 to 10, the surfaces gradually changed from relatively smooth and compact to rough, eroded and locally damaged. Progressive roughening and edge damage developed during repeated soaking and oven drying.

After two cycles, the specimens largely retained their cylindrical shape, and no extensive disintegration or large-scale spalling was observed. Non-carbonated and short-carbonated specimens showed small pores and slight colour differences, implying the onset of moisture migration and drying shrinkage. Specimens carbonated for 6–10 h retained clearer edges and lower erosion intensity. White surface deposits observed on some long-carbonated specimens were likely related to the migration and precipitation of alkaline salts or carbonate products.

After six and ten cycles, differences among carbonation durations became more apparent. The non-carbonated specimens displayed pronounced roughening, pore development and edge damage, while the 2 h and 4 h groups still showed local surface peeling and pore formation. The 6 h, 8 h and 10 h groups maintained better geometric integrity, and the 10 h group exhibited the least edge damage and the most stable side surface. These observations

demonstrate that sufficient carbonation improves resistance to wetting–drying-induced physical deterioration.

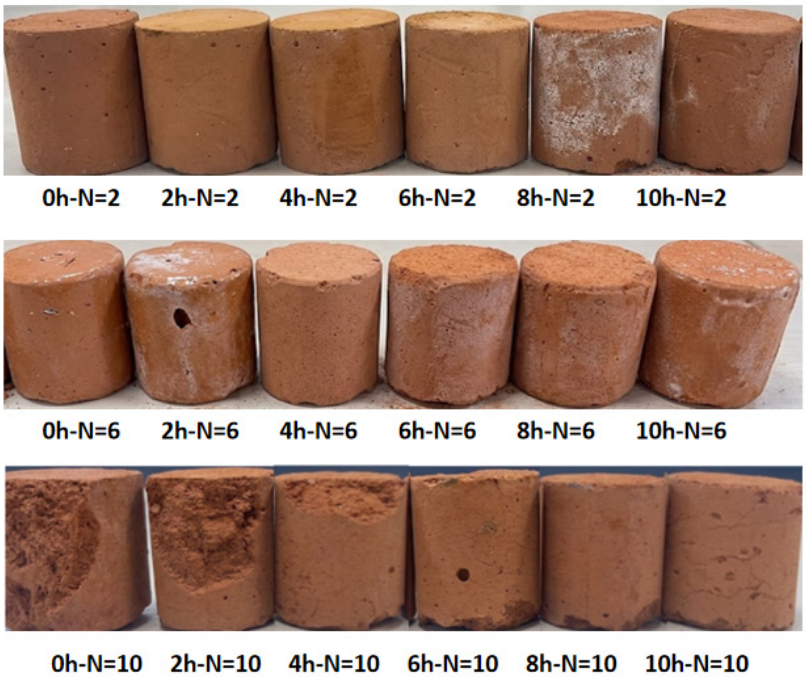


Figure 1. Surface morphology of carbonated red mud-based backfill specimens under wetting–drying cycles with carbonation durations of 0, 2, 4, 6, 8 and 10 h.

3.1.2. Red Mud Liquor Immersion

The macroscopic morphology after RML immersion is presented in Figure 2. In the specimen labels, the first value followed by "h" denotes the carbonation duration, and the second value followed by "d" denotes the subsequent RML immersion time. For example, "10h-28d" represents a specimen carbonated for 10 h and subsequently immersed in RML for 28 d. After 28 d of immersion, the specimens retained relatively complete cylindrical contours, and no through-cracks, extensive collapse, or large-scale block loss were observed. The dominant visible features were surface roughening, isolated pores, slight edge peeling, and limited white deposits.

The damage mechanism under continuous immersion differed from that under cyclic drying. Because the specimens remained wet during immersion, severe drying shrinkage stress did not develop. Instead, alkaline ions such as Na^+, OH^- and CO_3^{2-} migrated through the pore system and induced local softening, soluble component migration and limited particle loosening. The presence of light-coloured deposits also implies ion migration and salt/carbonate precipitation. These processes caused progressive surface degradation rather than rapid cracking.

Carbonation improved morphology retention during RML immersion. Carbonate crystals and activated reaction products filled pores and reduced the connectivity of liquid-transport paths. Consequently, the carbonated specimens maintained comparatively better surface integrity within the prescribed 28 d immersion period. Because the RML and wetting–drying protocols differed in exposure mode, duration, moisture history, and thermal action, the observations obtained from the two regimes were interpreted independently rather than converted into a common severity ranking.

Complete numerical results for mass variation, linear shrinkage, UCS, electrical resistivity, and pH are provided in Supplementary Tables S1–S5. These tables include the mean ± standard deviation, coefficient of variation, and percentage changes relative to the

specified reference conditions. Representative endpoint values and the principal trends are retained in the main text to facilitate interpretation.

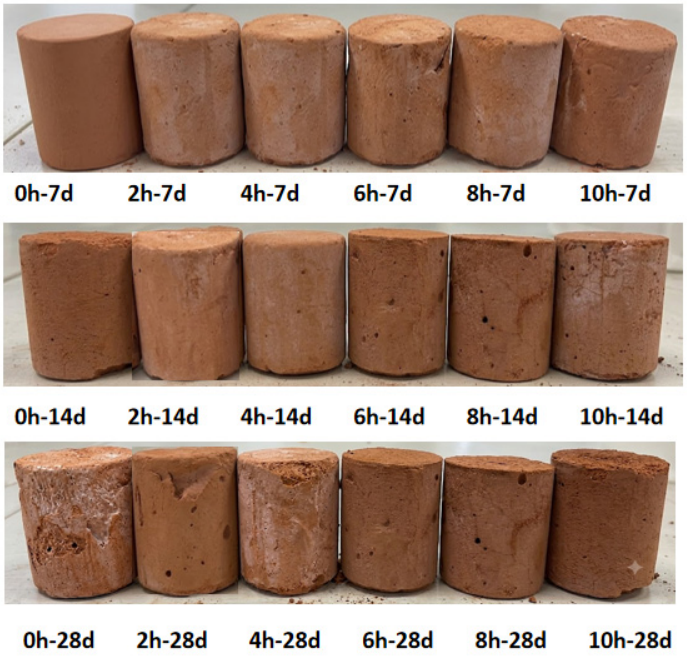
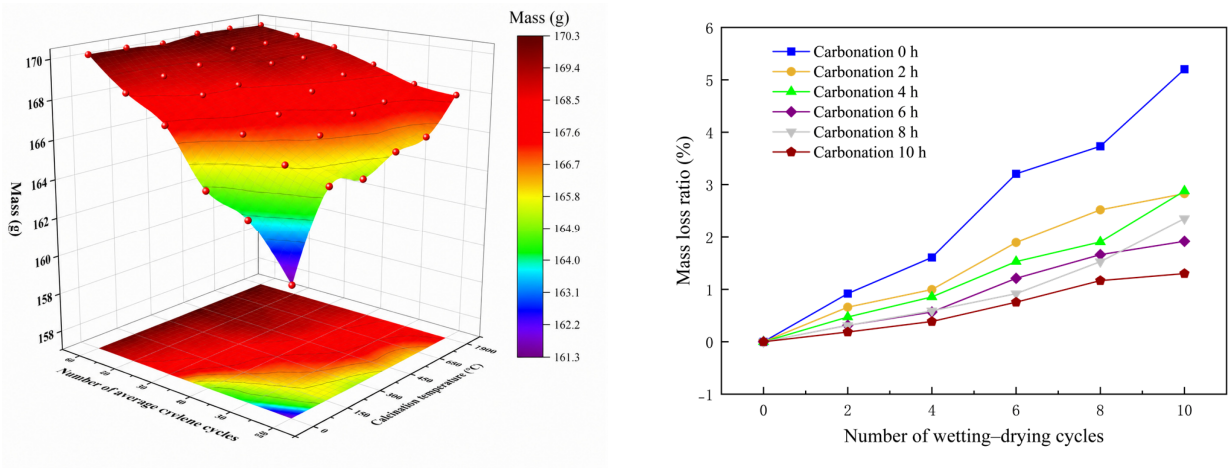


Figure 2. Macroscopic morphology of carbonated red mud-based backfill specimens after 7, 14, and 28 d of RML immersion.

3.2. Mass Loss and Shrinkage Response

3.2.1. Wetting–Drying Cycles

Mass evolution under wetting–drying cycles is shown in Figure 3. The complete mass and mass-loss data for both exposure regimes are listed in Supplementary Table S1. The specimen mass decreased gradually with increasing cycle number, while the mass loss ratio increased continuously. This trend indicates soluble component migration, surface particle loss and progressive internal structural damage during repeated soaking and drying. The non-carbonated specimens showed the greatest mass loss, whereas the carbonated specimens, particularly those carbonated for 8 h and 10 h, retained mass more effectively [33].



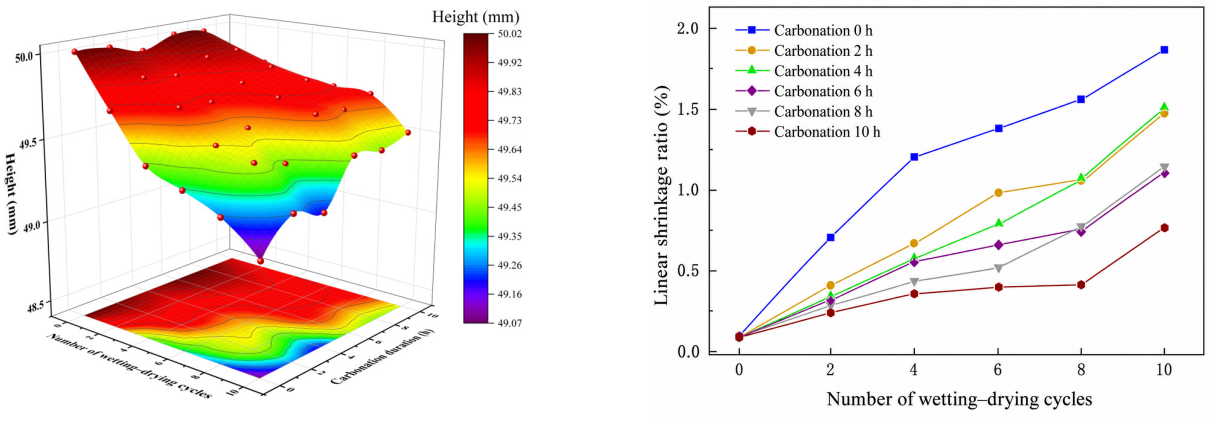
(**a**) (**b**)

Figure 3. Mass variation and mass loss ratio of specimens under wetting–drying cycles. (**a**) Response surface of mass variation. (**b**) Mass loss ratio.

After ten wetting–drying cycles, the mass-loss ratios of the 0, 2, 4, 6, 8, and 10 h carbonation groups were 5.20 ± 0.31%, 2.83 ± 0.16%, 2.88 ± 0.16%, 2.52 ± 0.13%, 2.35 ± 0.11%, and 1.30 ± 0.06%, respectively. The coefficients of variation ranged from 4.5% to 6.0%. The reduction was most pronounced between the non-carbonated and carbonated specimens, whereas the differences among the 2–8 h groups were comparatively smaller.

The different mass retention behaviour can be attributed to the evolution of hydration-carbonation products and pore structure. In non-carbonated specimens, MgO mainly formed $Mg(OH)_2$, and the cementation products were relatively insufficient to fill interparticle pores. During soaking, soluble alkaline components and weakly bonded particles could migrate outward; during drying, capillary shrinkage stresses promoted surface peeling and microcrack formation. After carbonation, magnesium carbonate phases and M-S-H/M-A-S-H gels filled pores, strengthened interparticle bonding and reduced pore connectivity, thereby suppressing material loss.

Height and linear shrinkage responses are shown in Figure 4. The corresponding height and linear-shrinkage data are provided in Supplementary Table S2. Specimen height decreased and linear shrinkage increased with cycle number. The non-carbonated group exhibited the largest shrinkage, whereas long-carbonated groups showed the smallest deformation. This indicates that carbonation not only reduces mass loss but also improves dimensional stability.



(**a**) (**b**)

Figure 4. Height variation and linear shrinkage ratio of specimens under wetting–drying cycles. (**a**) Response surface of specimen height. (**b**) Linear shrinkage ratio.

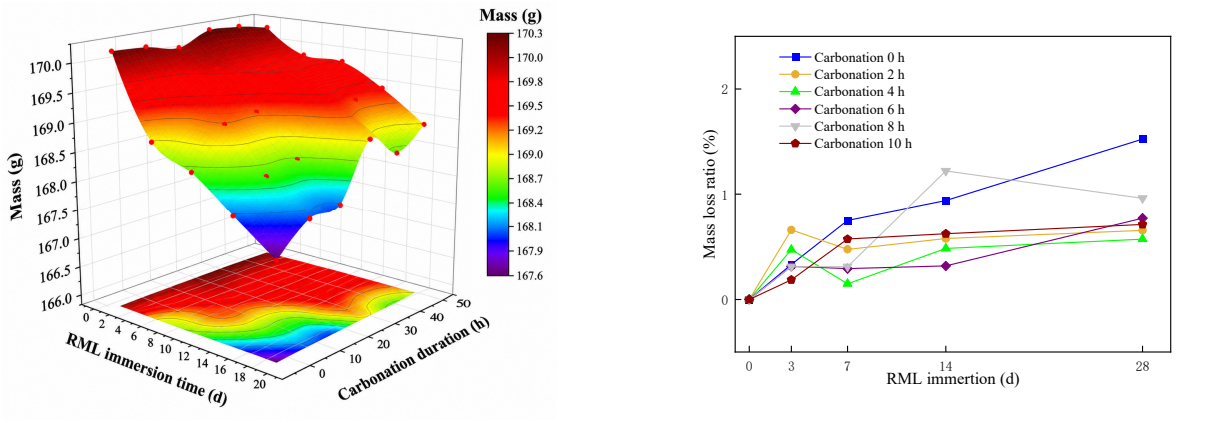
After ten cycles, the linear shrinkage ratios of the 0, 2, 4, 6, 8, and 10 h carbonation groups were 1.89 ± 0.11%, 1.48 ± 0.08%, 1.49 ± 0.08%, 1.08 ± 0.05%, 1.10 ± 0.05%, and 0.71 ± 0.03%, respectively. The corresponding coefficients of variation ranged from 4.5% to 5.8%. The 6–10 h groups therefore maintained lower dimensional changes than the non-carbonated and short-carbonated specimens within the investigated cycle range.

Shrinkage was mainly caused by softening of weakly bonded zones during soaking and capillary/drying shrinkage during oven drying. The carbonate-gel skeleton formed through carbonation limited particle rearrangement, restrained pore compression and reduced moisture-migration disturbance, resulting in lower linear shrinkage after cyclic exposure.

3.2.2. Red Mud Liquor Immersion

Mass variation under RML immersion is shown in Figure 5. The overall mass change was limited, and no severe collapse or large-scale peeling occurred. With immersion time increasing to 28 d, mass loss increased slowly, indicating gradual soluble component migration, slight surface erosion and local cementation damage. The non-carbonated group

exhibited higher mass loss than the carbonated groups, while the 4–10 h carbonation groups showed better mass stability.

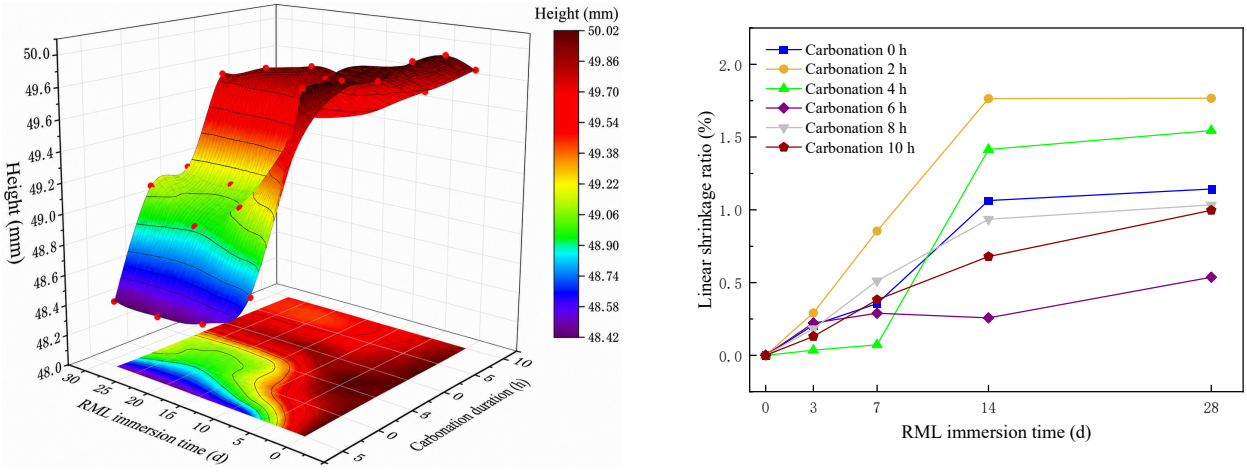


(**a**) (**b**)

Figure 5. Mass variation and mass-loss ratio of specimens during RML immersion. (**a**) Mass variation. (**b**) Mass loss ratio.

At early immersion ages, some fluctuations in mass loss were observed. This may be associated with continued MgO hydration and alkaline activation of active Si and Al components from CFB ash. New gel products generated in this stage could partly fill pores and temporarily restrain mass loss. With longer immersion, sustained ion migration and local dissolution or reorganization of cementitious products caused gradual mass loss.

Figure 6 presents the height and linear-shrinkage evolution during RML immersion. The measured height change was limited, and the linear shrinkage remained low throughout the 28 d immersion period. Because continuous immersion did not involve repeated drying, the specimens were not subjected to cyclic drying-shrinkage stress. Their deformation was mainly associated with prolonged softening, pore rearrangement, and limited particle migration. The longer-carbonated specimens showed lower shrinkage within the investigated immersion period, indicating improved dimensional retention after carbonation. These values characterize the response under the prescribed RML protocol and are not used to establish an equivalent exposure severity relative to wetting–drying cycling.



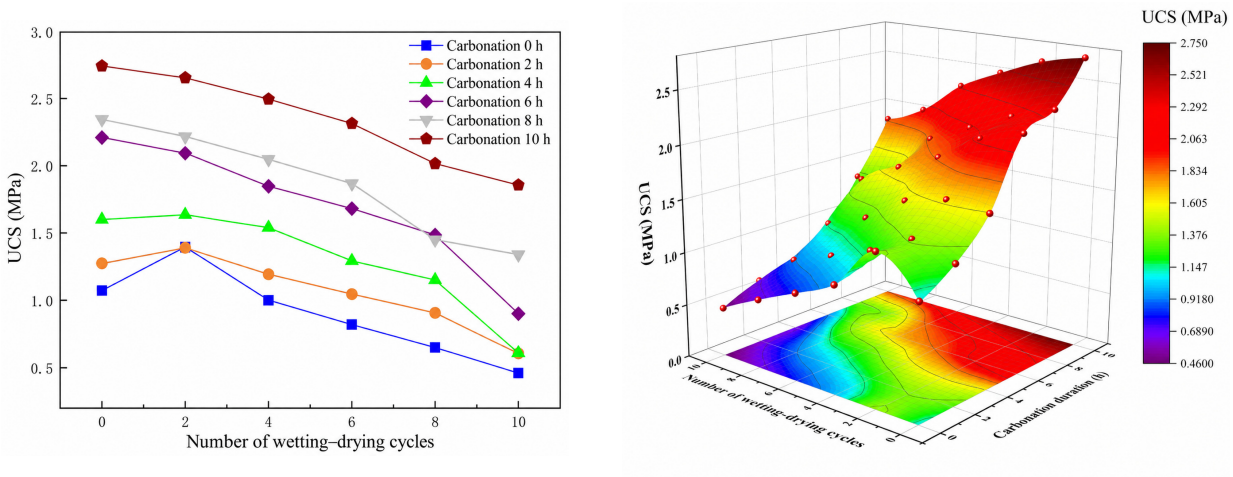
(**a**) (**b**)

Figure 6. Height variation and linear-shrinkage ratio of specimens during RML immersion. (**a**) Response surface of specimen height. (**b**) Linear shrinkage ratio.

3.3. Unconfined Compressive Strength

3.3.1. Wetting–Drying Cycles

The UCS evolution under wetting–drying cycles is shown in Figure 7. The complete UCS dataset for the wetting–drying and RML immersion conditions is provided in Supplementary Table S3. Before cyclic exposure, UCS generally increased with carbonation duration. The 10 h carbonation group showed the highest initial strength, followed by the 8 h and 6 h groups, whereas the non-carbonated and short-carbonated groups showed lower strength. This trend indicates that carbonation was associated with improved initial load-bearing capacity.



(**a**) (**b**)

Figure 7. Unconfined compressive strength of specimens under wetting–drying cycles. (**a**) UCS evolution. (**b**) UCS response surface.

After ten wetting–drying cycles, the UCS values of the 0, 2, 4, 6, 8, and 10 h groups were 0.460 ± 0.030, 0.605 ± 0.038, 0.609 ± 0.037, 0.901 ± 0.050, 1.340 ± 0.070, and 1.856 ± 0.089 MPa, respectively. The coefficients of variation ranged from 4.8% to 6.5%, with slightly greater dispersion in the specimens subjected to shorter carbonation durations. The 10 h group retained 67.7% of its initial strength, compared with 42.9% for the non-carbonated group.

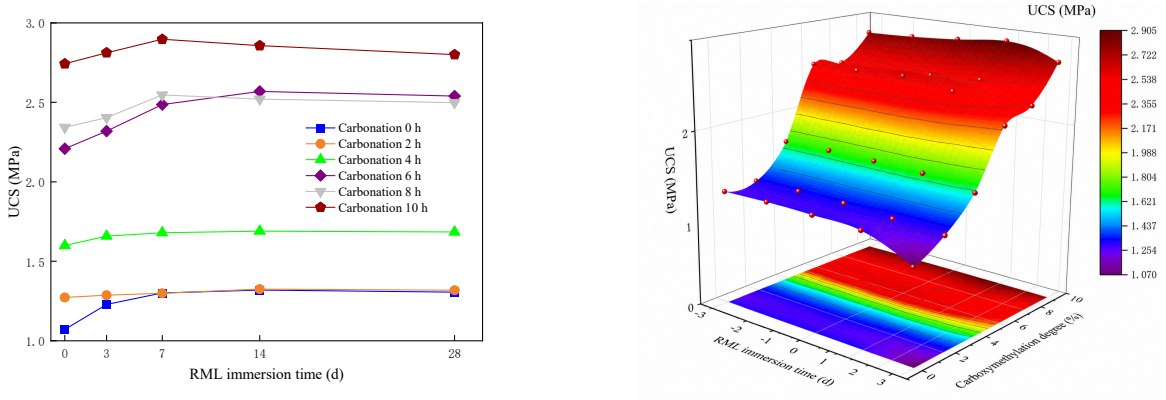
With increasing cycle number, UCS generally decreased, but the degradation rate depended strongly on carbonation duration. Non-carbonated and 2 h carbonated specimens exhibited local fluctuations in the early cycles, probably due to continued hydration of unreacted MgO and further activation of CFB ash. At later cycles, softening, soluble component loss and microcrack propagation became dominant, leading to strength decline. The 6–10 h carbonation groups possessed a more mature carbonate-gel skeleton and therefore retained higher residual strength throughout cyclic exposure.

The specimens generally exhibited axial splitting or mixed splitting–shear failure. After repeated cycling, local crushing and fragment detachment were more evident in the non-carbonated and short-carbonated specimens, whereas the longer-carbonated groups retained comparatively more coherent fragments after failure.

The response surface in Figure 7b shows that UCS increased with carbonation time but decreased with wetting–drying cycles. The high-strength region was concentrated at long carbonation duration and low cycle number, while the low-strength region occurred at short carbonation duration and high cycle number. Thus, carbonation duration affected both the initial strength and its retention during cyclic exposure.

3.3.2. Red Mud Liquor Immersion

UCS during RML immersion is shown in Figure 8. The measured UCS generally increased with carbonation duration. The non-carbonated and 2 h carbonated groups showed comparatively lower values, the 4 h group exhibited an intermediate response, and the 6, 8, and 10 h groups retained higher UCS throughout the tested immersion period. Among the investigated groups, the 10 h carbonation specimens maintained the highest mean UCS.



(**a**) (**b**)

Figure 8. Unconfined compressive strength of specimens during RML immersion. (**a**) UCS evolution. (**b**) UCS response surface.

During the 28 d RML immersion period, UCS did not decrease continuously. Most groups showed an increase during the first 7 d, followed by stabilization or a slight reduction at later ages. The early increase was associated with continued reaction and alkaline activation: OH^- in the red mud liquor promoted the dissolution of reactive Si- and Al-bearing components in CFB ash and red mud, contributing to the formation of additional binding products. These products filled pores and increased interparticle bonding. Between 14 and 28 d, local dissolution, ion exchange, and product reorganization became more evident, causing strength development to level off or decline slightly.

The RML-exposed specimens mainly exhibited axial splitting and mixed splitting–shear failure. No systematic change in the dominant failure pattern was observed within the 28 d immersion period, although the short-carbonated specimens showed greater local fragmentation after loading.

3.3.3. Coupled Strength Models

The fitted strength surface for wetting–drying cycles is shown in Figure 9. The model captures the overall distribution of experimental values. UCS increased along the carbonation-time direction and decreased along the cycle-number direction [34]. The gentler decline in long-carbonated specimens demonstrates that sufficient carbonation suppresses cyclic damage [35–37].

For RML immersion, the fitted surface is shown in Figure 10. The strength surface reflects the combined effects of carbonation enhancement, early alkaline activation and long-term erosion. Strength increased markedly with carbonation time and exhibited a rise-stabilization trend along immersion time. The fitting result supports the view that RML immersion is not purely corrosive at early ages; it can also promote secondary reactions in the alkaline environment.

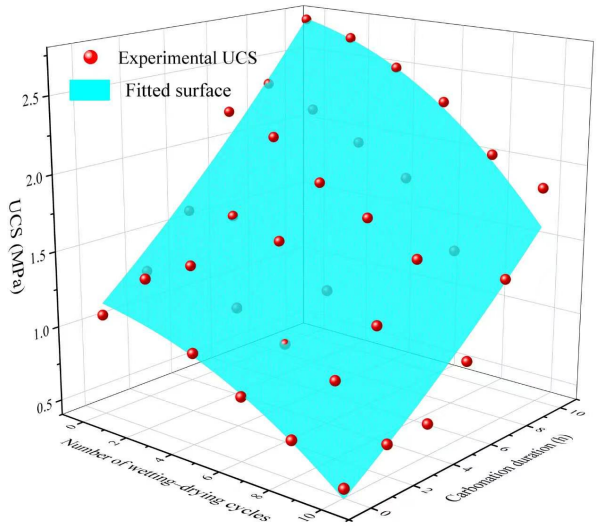


Figure 9. Experimental UCS values and fitted surface under coupled carbonation time and wetting–drying cycle number.

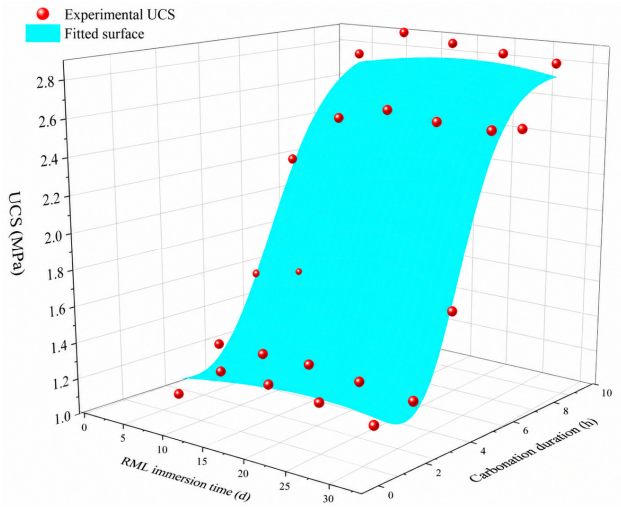


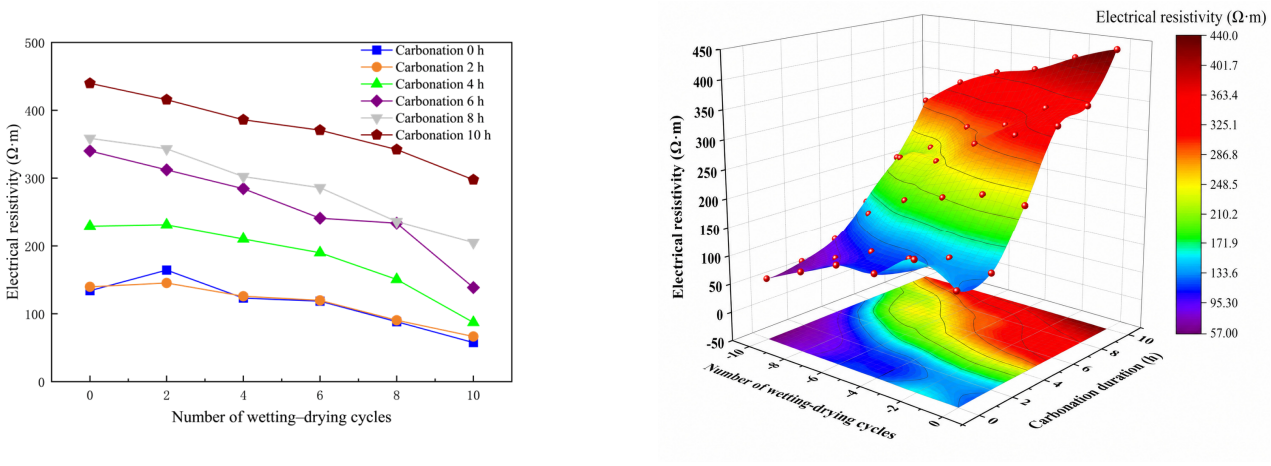
Figure 10. Experimental UCS values and fitted surface under coupled carbonation time and red mud liquor immersion time.

3.4. Electrical Resistivity

3.4.1. Wetting–Drying Cycles

Electrical resistivity under wetting–drying cycles is shown in Figure 11. The corresponding electrical-resistivity data are listed in Supplementary Table S4. Before cyclic exposure, resistivity increased with carbonation duration, following the same trend as UCS. This trend is consistent with reduced pore connectivity and restricted ion migration pathways after carbonation. Under wetting–drying cycles, resistivity decreased with increasing cycles, particularly in short-carbonated specimens. The decline reflects microcrack formation, cementation product debonding and reconnection of pores.

After ten wetting–drying cycles, the electrical resistivity values of the 0, 2, 4, 6, 8, and 10 h groups were 57.52 ± 3.57, 66.46 ± 3.99, 87.23 ± 5.06, 138.64 ± 7.49, 205.04 ± 10.25, and 297.55 ± 13.69 Ω·m, respectively. The coefficients of variation ranged from 4.6% to 6.2%. The 10 h group retained approximately 67.7% of its initial resistivity, whereas the non-carbonated group retained 42.9%, which is consistent with the corresponding UCS response.



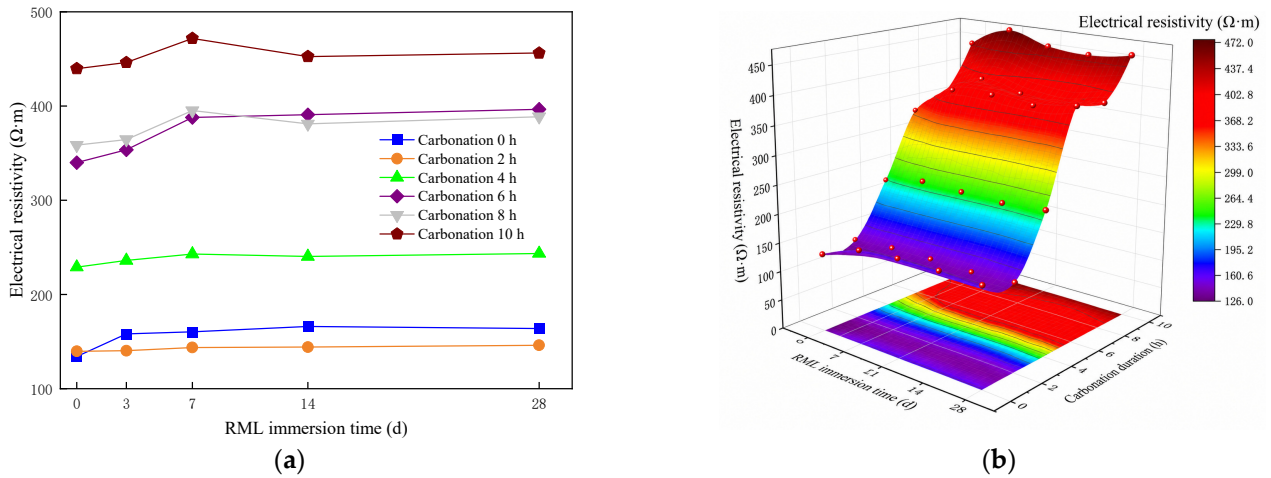
(**a**) (**b**)

Figure 11. Electrical resistivity of specimens under wetting–drying cycles. (**a**) Resistivity evolution. (**b**) Resistivity response surface.

Because all wetting–drying specimens were measured after the prescribed 60 °C drying stage and cooling to 20 ± 2 °C, the moisture-conditioning history was kept consistent within this exposure regime. The measured resistivity was therefore interpreted as a comparative indicator of pore connectivity and structural integrity rather than as an intrinsic material constant. Its general agreement with mass loss, linear shrinkage, and UCS supports the use of electrical resistivity as an auxiliary index for tracking wetting–drying deterioration under the specified laboratory conditions.

3.4.2. Red Mud Liquor Immersion

Electrical resistivity during RML immersion is shown in Figure 12. Resistivity generally increased with carbonation duration, which is consistent with reduced pore connectivity and improved structural compactness after carbonation. Along the immersion-time direction, resistivity increased at early ages and subsequently stabilized or fluctuated slightly. This response was consistent with continued reaction and pore filling during early immersion, followed by local reorganization or dissolution of cementitious products. No abrupt decrease in resistivity occurred within 28 d, suggesting that electrical integrity was largely retained within the investigated immersion interval.



(**a**) (**b**)

Figure 12. Electrical resistivity of specimens during RML immersion. (**a**) Resistivity evolution. (**b**) Resistivity response surface.

Because the RML-exposed specimens retained internal moisture and pore solution after surface blotting, the measured resistivity reflected the combined effects of pore connectivity, residual moisture, and pore-solution chemistry. The values were therefore used to compare carbonation groups and immersion ages within the RML regime, rather than for direct comparison with the absolute resistivity values measured after wetting–drying exposure.

3.4.3. Correlation Between Resistivity and Strength

Figures 13 and 14 show the relationship between electrical resistivity and UCS. To quantify this relationship, ordinary least-squares linear regression was performed separately for the wetting–drying and RML immersion datasets. The fitting function was expressed as $q_u = a\rho + b$, where q_u is the unconfined compressive strength, ρ is the electrical resistivity, and a and b are the fitted slope and intercept, respectively. All carbonation-duration and exposure-level data within the same exposure regime were included in the corresponding regression. Separate fitting was adopted because the wetting–drying and RML specimens were tested under different moisture-conditioning and pore-solution conditions. For each carbonation group, resistivity was positively correlated with UCS. This correlation arises because both indices are controlled by pore structure, quantity of cementation products, crack connectivity and skeleton continuity. When carbonate crystals and gels fill the pores, the specimens become denser and stronger, and resistivity increases. When wetting–drying or chemical erosion damages cementation products and increases pore connectivity, strength and resistivity decline or grow more slowly [38].

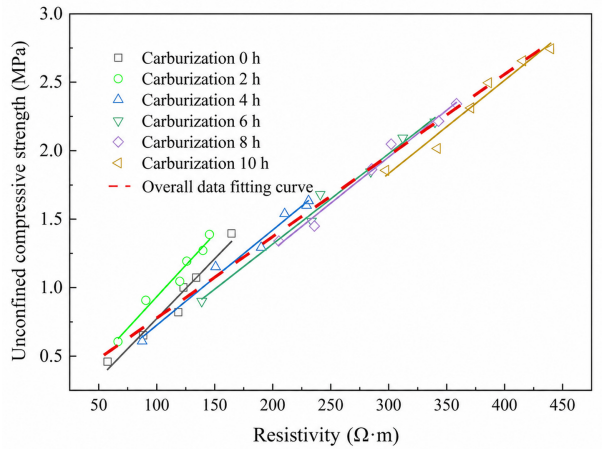


Figure 13. Relationship between electrical resistivity and UCS under wetting–drying cycles.

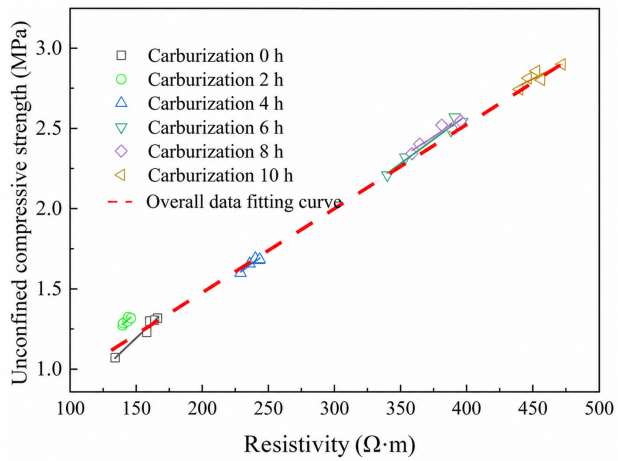


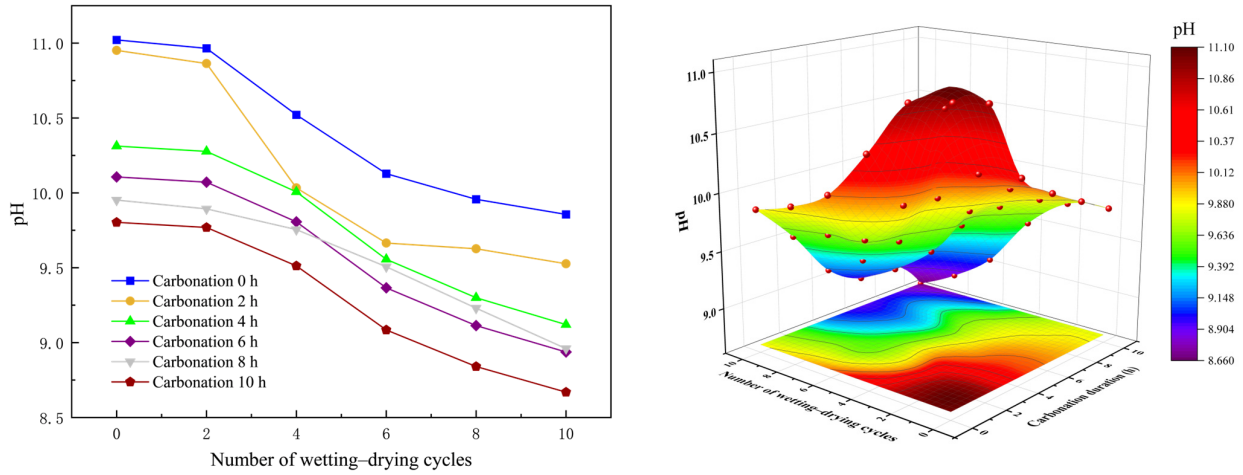
Figure 14. Relationship between electrical resistivity and UCS under red mud liquor immersion.

Resistivity testing is rapid and less destructive than UCS testing. It can therefore be used as a practical supplementary method to assess the structural integrity and service state of carbonated red mud-based backfill.

3.5. Environmental Performance

3.5.1. pH Evolution

The pH evolution under wetting–drying cycles is shown in Figure 15. The complete pH dataset for both exposure regimes is provided in Supplementary Table S5. pH decreased with both cycle number and carbonation duration. The non-carbonated specimens had the highest initial pH, indicating higher retained alkalinity. Increasing carbonation time consumed OH^- and $Mg(OH)_2$ through CO_2 reaction and produced carbonate phases, thereby reducing pH. During cyclic exposure, soluble alkaline ions such as Na^+ and OH^- migrated outward during soaking, and salt redistribution occurred during drying, causing additional pH reduction.



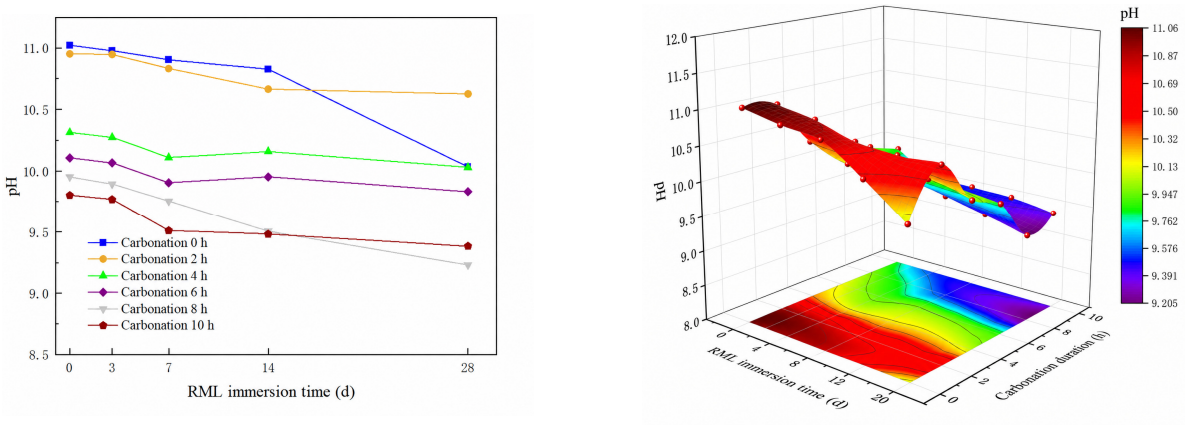
(**a**) (**b**)

Figure 15. pH of specimens under wetting–drying cycles. (**a**) pH evolution. (**b**) pH response surface.

After ten wetting–drying cycles, the pH values of the 0, 2, 4, 6, 8, and 10 h groups were 9.86 ± 0.08, 9.53 ± 0.08, 9.12 ± 0.06, 8.94 ± 0.06, 8.96 ± 0.05, and 8.67 ± 0.05, respectively. The coefficients of variation ranged from 0.6% to 0.8%, showing relatively limited dispersion among the parallel measurements. The overall pH reduction reflected both carbonation-induced alkalinity consumption and the continued migration of soluble alkaline constituents during cyclic exposure.

The decrease in pH should not be interpreted as direct evidence of structural deterioration. In MgO-based carbonated systems, lower pH also reflects conversion of alkaline components into stable carbonate products. Long-carbonated specimens had lower pH but better strength, resistivity and dimensional stability, indicating that durability was mainly governed by pore filling and skeleton integrity rather than alkalinity alone.

The pH response under RML immersion is presented in Figure 16. pH generally decreased with immersion time and carbonation duration. The decrease was associated with leaching of soluble alkaline ions, reactions between RML ions and pore solution components, and reorganization of hydration-carbonation products. Again, the low-pH region did not correspond to the low-strength region, suggesting that pH should be used as an indicator of chemical environment evolution rather than as a single durability criterion.



(**a**) (**b**)

Figure 16. pH of specimens under red mud liquor immersion. (**a**) pH evolution. (**b**) pH response surface.

3.5.2. Hazardous-Element Leaching

Hazardous-element leaching results after wetting–drying cycles and RML immersion are summarized in Tables 2 and 3. In both environments, leaching concentrations were low. Na showed higher values than other elements because of the high sodium content and alkalinity of red mud, but the measured values remained below the adopted limit. As, Hg, Pb and Cu were not detected or were below the reporting threshold, and Cd was only detected at very low concentrations [39,40]. Under the specified extraction conditions, the measured concentrations of the target elements were below the adopted comparison values. These results characterize the laboratory leaching response of the tested material and should not be interpreted as direct estimates of long-term field-scale mass release.

Table 2. Hazardous-element leaching results after wetting–drying cycles (mg/L).

Item	Na	As	Hg	Cd	Pb	Cu
Limit	200	0.01	0.001	0.003	0.001	2
Backfill leachate	17.6	<LOD	<LOD	0.0002	<LOD	<LOD

Note: Values are reported as the means of three independent extracts. <LOD indicates a concentration below the corresponding method detection limit. Method blanks were below the detection limits for all target elements.

Table 3. Hazardous-element leaching results after red mud liquor immersion (mg/L).

Item	Na	As	Hg	Cd	Pb	Cu
Limit	200	0.01	0.001	0.003	0.001	2
Backfill leachate	8.7	<LOD	<LOD	0.0003	<LOD	<LOD

Note: Values are reported as the means of three independent extracts. <LOD indicates a concentration below the corresponding method detection limit. Method blanks were below the detection limits for all target elements.

The low leaching risk can be attributed to the composite immobilization effect of carbonate crystals and gel products. Carbonation products fill pores and reduce migration pathways, while M-S-H, M-A-S-H, C-A-S-H and N-A-S-H gels provide adsorption, ion-exchange, surface complexation and physical encapsulation sites. In alkaline environments, some metal ions may also be stabilized as hydroxide, carbonate or aluminosilicate-associated forms. Therefore, despite physical damage or ion migration, the carbonated solidified system maintained good environmental safety.

3.6. Microstructural Evolution

3.6.1. SEM Observations

SEM images under wetting–drying cycles are shown in Figure 17. For the 4 h carbonation group after two cycles, cementation products were present but the pore structure remained obvious, and local large pores and loose zones were observed. After eight cycles, pores expanded, connected cracks developed and interparticle bonding weakened. In contrast, the 8 h carbonation group exhibited a denser structure after two cycles, with more continuous cementation products. After eight cycles, local pore enlargement and microcracks also appeared, but the overall integrity remained superior to that of the 4 h group [41].

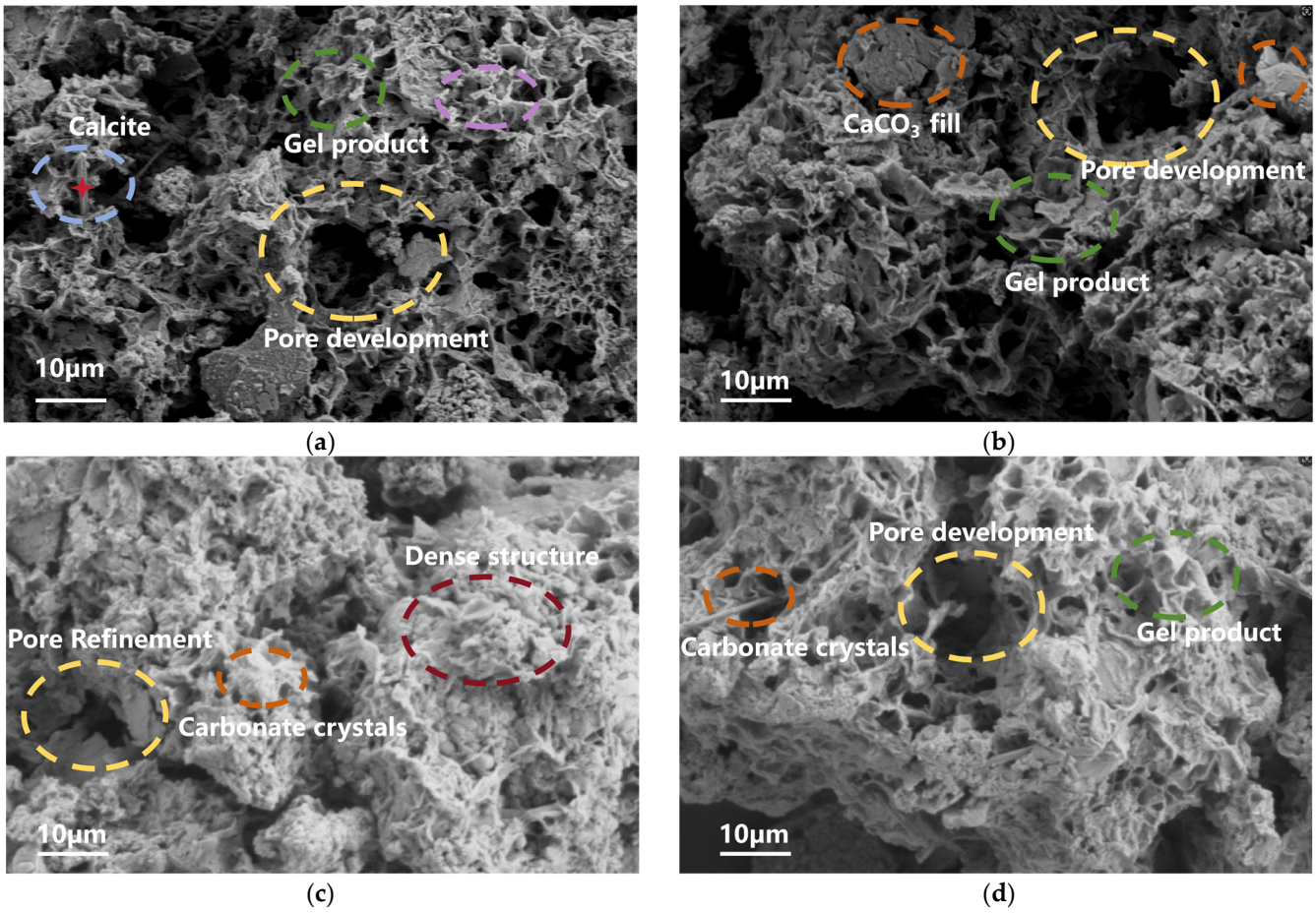


Figure 17. SEM images of specimens after wetting–drying cycles: (**a**) 4 h carbonation, N = 2; (**b**) 4 h carbonation, N = 8; (**c**) 8 h carbonation, N = 2; and (**d**) 8 h carbonation, N = 8.

These SEM observations are consistent with the macroscopic performance trends and provide qualitative evidence of changes in pore morphology and cemented-skeleton continuity. The short-carbonated specimens exhibited more open pores, product debonding, and pore reconnection after cyclic exposure, corresponding to their larger mass loss and shrinkage and lower residual UCS and resistivity. The longer-carbonated specimens retained a comparatively more continuous cemented skeleton, which is consistent with their improved mechanical and dimensional retention.

SEM images after RML immersion are presented in Figure 18. Short-term immersion specimens contained abundant gel-like products. When considered together with the XRD results, these features were consistent with the continued formation of low-crystallinity binding products. With prolonged immersion, needle-like or plate-like crystalline products appeared in local pores, suggesting ion participation and crystal precipitation. At early

immersion ages, gel-like products and local pore filling coincided with the measured increases in UCS and electrical resistivity. At later ages, enlarged pores, local cracks, and weakened interfaces were consistent with the stabilization or slight decline in these properties and the gradual increase in mass loss. Taken together with the XRD results discussed in Section 3.6.2, these observations support a staged response from early continued reaction and pore filling to later local dissolution, product reorganization, and interface weakening.

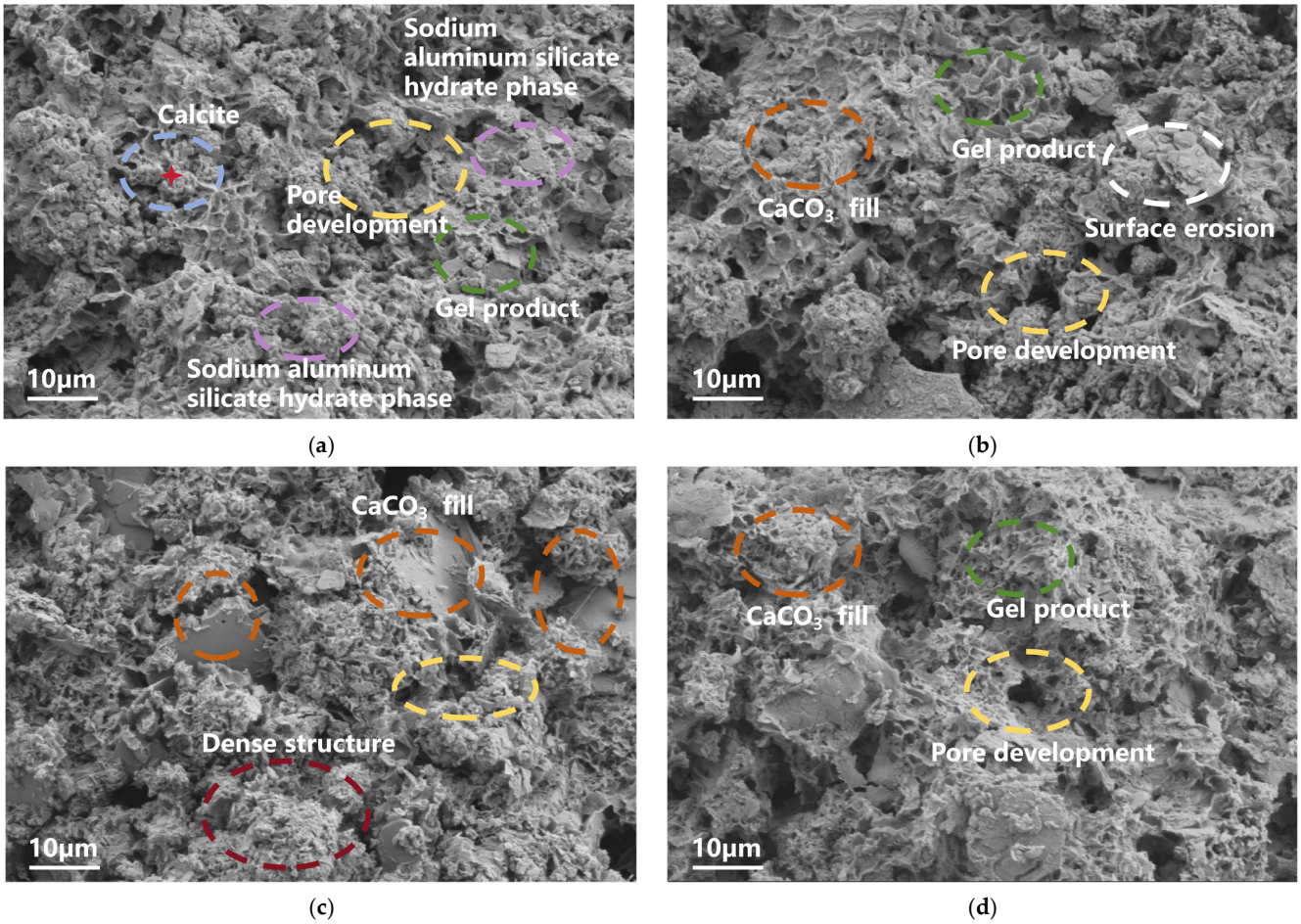


Figure 18. SEM images of specimens after red mud liquor immersion: (**a**) 4 h carbonation, 3 d; (**b**) 4 h carbonation, 28 d; (**c**) 8 h carbonation, 3 d; and (**d**) 8 h carbonation, 28 d.

3.6.2. XRD Analysis

XRD patterns after wetting–drying cycles are shown in Figure 19. The main diffraction peak positions remained essentially unchanged, indicating that wetting–drying cycles did not alter the dominant phase assemblage. The identifiable phases/products included primary SiO_2, $Mg(OH)_2$, $CaCO_3$, hydrated magnesium carbonates, and low-crystallinity C-S-H/C-A-S-H-type products. For 2 h carbonation, the carbonate peak near 29.4° increased after additional cycles, implying that short-carbonated specimens still had unreacted $Mg(OH)_2$ and active components that could continue reacting [42]. For 8 h carbonation, stronger carbonate peaks were already present at early cycles, demonstrating a more complete carbonated structure. At later cycles, partial peak weakening suggested damage or reorganization of gel and carbonate products.

XRD patterns after RML immersion are shown in Figure 20. The main phase types remained stable, including Fe_2O_3, $Al(OH)_3$, SiO_2, $CaCO_3$, $CaSO_4{\cdot}2H_2O$, MgO, C-A-S-H and N-A-S-H-related products. Fe_2O_3 and SiO_2 mainly originated from stable mineral phases in red mud and CFB ash, while carbonate phases were associated with carbonation

reactions. The presence of C-A-S-H and N-A-S-H indicates that the alkaline RML environment promoted further reaction of active Si and Al components. Changes in relative peak intensities suggest simultaneous secondary reaction and local product reorganization.

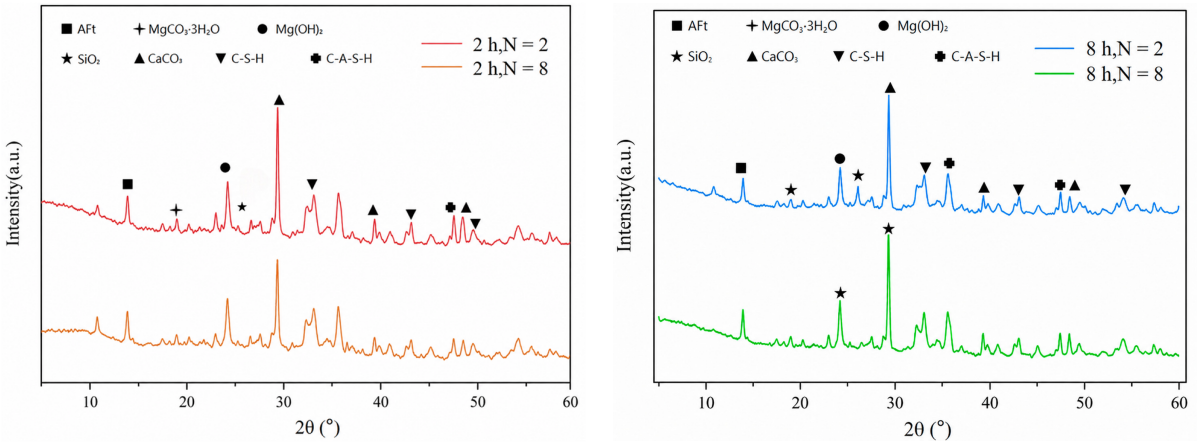


Figure 19. XRD patterns of specimens after wetting–drying cycles. (**a**) The 2 h carbonation. (**b**) The 8 h carbonation.

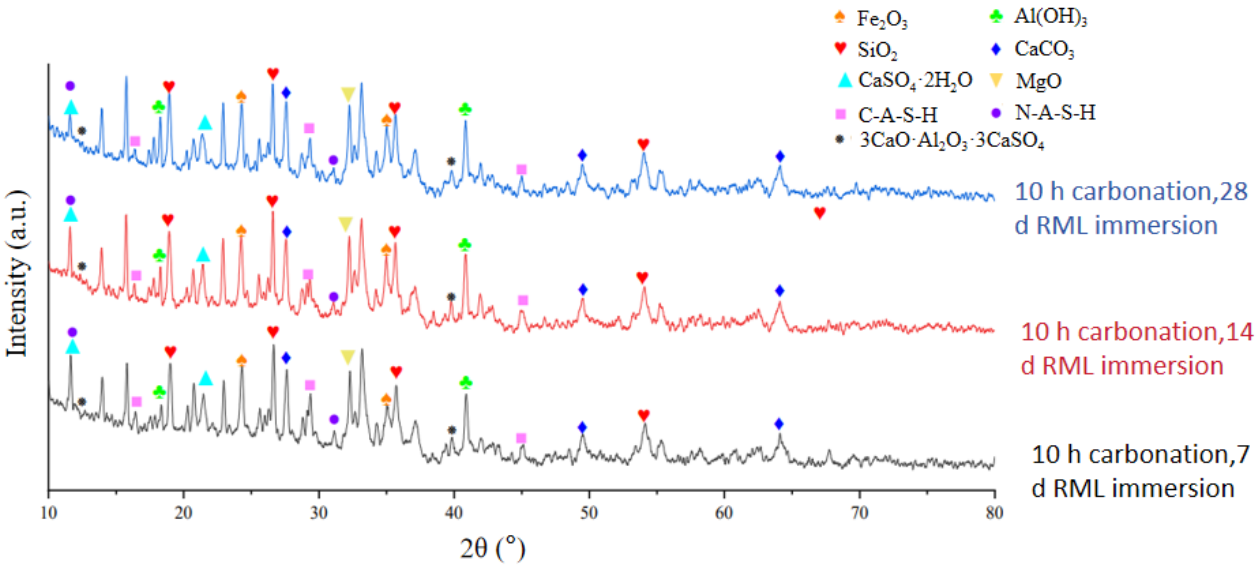


Figure 20. XRD patterns of specimens after red mud liquor immersion.

The XRD results were used to identify the principal crystalline phases and support the interpretation of phase evolution. Quantitative phase fractions were not determined in the present study; therefore, the contribution of each reaction product is discussed qualitatively. An uncarbonated reference pattern would provide a useful baseline for evaluating carbonation-induced phase changes. However, an equivalent uncarbonated specimen with the same preparation and exposure history was not included in the retained sample set. To maintain the comparability of the XRD results, the present discussion is restricted to the available carbonated specimens.

4. Discussion

4.1. Strength-Threshold Estimation and Model Limitations

For practical evaluation, a quadratic response surface was adopted to describe UCS as a function of carbonation time and wetting–drying cycle number [43,44]:

$$q_u(N, t_c) = \beta_0 + \beta_1 t_c + \beta_2 N + \beta_3 t_{(c^2)} + \beta_4 N^2 + \beta_5 t_c N \tag{12}$$

$$q_u(N, t_c) = 1.1804 + 0.1028 t_c - 0.000593 N + 0.005603 t_{(c^2)} - 0.007855 N^2 - 0.003032 t_c N \tag{13}$$

$$q_u(N^f, t_c) = q_{cr} \tag{14}$$

$$\beta_4 N^f 2 + (\beta_2 + \beta_5 t_c) N^f + (\beta_0 + \beta_1 t_c + \beta_3 t_{(c^2)} - q_{cr}) = 0 \tag{15}$$

For the wetting–drying dataset, the model gave R^2 = 0.9722 and RMSE = 0.1008 MPa, indicating good fitting quality. With a critical strength q_{cr} = 0.8 MPa, the predicted wetting–drying service lives are listed in Table 4.

Table 4. Model-estimated strength-threshold exposure under wetting–drying cycles.

Carbonation Time/h	Estimated Threshold Exposure/Cycles	Life Increase Relative to 0 h/%
0	6.92	0
2	8.39	21.18
4	9.81	41.77
6	11.22	62.05
8	12.60	82.11
10	13.98	102.05

The predicted equivalent life increased from 6.92 cycles for the non-carbonated group to 13.98 cycles for the 10 h carbonation group, corresponding to a 102.05% increase. The life increase was more rapid between 0 and 6 h and became slower between 8 and 10 h, indicating that the carbonation benefit gradually approached a stable state.

For RML immersion, the quadratic response surface was:

$$q_u(T_a,\ t_c) = 1.0271 + 0.1647 t_c + 0.02194 T_a + 0.001004 t_c^2 - 0.000589 T_a^2 - 0.0001377 t_c T_a \tag{16}$$

The fitting quality was R^2 = 0.9332 and RMSE = 0.1592 MPa. Using q_{cr} = 0.8 MPa, the predicted RML immersion lives are listed in Table 5.

Table 5. Model-estimated strength-threshold time under RML immersion.

Carbonation Duration (h)	Estimated Threshold Time (d)	Increase Relative to 0 h (%)
0	45.69	0.00
2	54.12	18.45
4	60.66	32.78
6	66.13	44.74
8	70.86	55.09
10	75.05	64.26

The model-estimated strength-threshold time increased from 45.69 d for the non-carbonated group to 75.05 d for the 10 h carbonation group, corresponding to an increase of 64.26%. The increase resulted from the combined effects of a higher initial UCS and a lower subsequent rate of strength reduction in the longer-carbonated specimens. These values describe the relative strength retention of the different carbonation groups under the prescribed RML immersion condition.

A strength-based life damage variable can be defined as:

$$D^L(T_a,\ t_c) = [q_u(0,\ t_c) - q_u(T_a,\ t_c)] / [q_u(0,\ t_c) - qc_r] \tag{17}$$

$$R^L(T_a,\ t_c) = 1 - D^L(T_a,\ t_c) \tag{18}$$

where D^L is the life damage variable and R^L is the remaining-life coefficient. $D^L = 0$ indicates no strength damage, whereas $D^L = 1$ indicates that the strength has reached the critical limit. A higher R^L indicates a larger remaining service life.

A second-order response surface was adopted because the UCS data exhibited curvature with both carbonation duration and exposure level. The quadratic form represented the main effects and their interaction without introducing higher-order terms unsupported by the available dataset. The wetting–drying model yielded $R^2 = 0.972$ and an RMSE of 0.1008 MPa, whereas the RML model yielded $R^2 = 0.9332$ and an RMSE of 0.1592 MPa. These values indicate that the fitted surfaces adequately describe the measured strength trends within the investigated ranges.

The UCS threshold of $q_{cr} = 0.8$ MPa was applied consistently to compare the relative strength retention of specimens with different carbonation durations. It was adopted as a common model-based comparison criterion and is not presented as a code-prescribed failure limit or a universal engineering design value.

The values reported in Tables 4 and 5 are strength-threshold estimates derived from the fitted response surfaces. They are used to compare the relative strength retention of specimens subjected to different carbonation durations under the specified laboratory exposure regimes and do not represent directly verified field service lives. Because the two exposure regimes differed in moisture history, thermal action, and solution chemistry, their threshold estimates were interpreted separately and were not assigned direct field-time equivalents. For the wetting–drying condition, the estimated threshold values remain close to the range covered by the cyclic tests. For RML immersion, however, the experimental period was limited to 28 d, whereas the calculated threshold times ranged from 45.69 to 75.05 d. The RML results therefore represent extrapolations beyond the measured interval and are valid only under the assumptions of the fitted model and the adopted UCS threshold of 0.8 MPa. Field temperature, degree of saturation, stress state, seepage rate, solution renewal, seepage chemistry, and loading history may alter the actual deterioration rate. Accordingly, the results are interpreted as relative comparisons among carbonation groups within each laboratory exposure regime rather than as direct predictions of field service duration.

The microstructural interpretation associated with the strength evolution was established from the combined SEM and XRD results. The observed carbonate-bearing crystalline phases, gel-like products, pore filling, and local pore development support the proposed sequence of carbonation-induced densification followed by exposure-related structural deterioration. Because the low-crystallinity reaction products were identified from morphological features and phase assemblages rather than quantitatively resolved as individual gel phases, the microstructural results are used to explain the measured performance trends without assigning a unique contribution to each reaction product. Accordingly, the models in this section are applied to evaluate relative durability trends and strength-threshold exposure levels within the investigated material system.

The cylindrical specimens used in this study had a height-to-diameter ratio of 1.0, which differs from the ratio of 2.0 commonly adopted in some cemented-backfill strength tests. Because specimen geometry can influence the measured UCS, the absolute strength values and fitted strength-threshold estimates should be interpreted within the present constant-geometry experimental system. Direct conversion to results obtained from 50 mm × 100 mm specimens was not attempted.

4.2. Mechanistic Interpretation

The protective effect of carbonation can be interpreted through several complementary pathways. Carbonate-bearing crystalline phases and gel-like reaction products occu-

pied interparticle pores and reduced the continuity of moisture- and ion-transport paths. Meanwhile, the more continuous cemented skeleton improved interparticle bonding and restrained particle rearrangement, shrinkage, and crack development. These structural changes were consistent with the higher UCS and electrical resistivity and the lower mass loss and linear shrinkage observed in the longer-carbonated specimens.

The two exposure regimes produced distinct deterioration responses. Wetting–drying cycling in deionized water was dominated by moisture migration, drying shrinkage, product debonding, and microcrack development; alkaline filtrate may additionally promote ion migration and salt crystallization. By contrast, RML immersion involved sustained alkaline transport, local dissolution, precipitation, and product reorganization. These interpretations are qualitatively supported by the macroscopic, SEM, and XRD observations, although quantitative pore-size distribution and phase composition were not determined in the present study.

5. Conclusions

(1) Increasing carbonation duration improved resistance to wetting–drying deterioration. After ten cycles, the 10 h carbonation group exhibited a mass-loss ratio of 1.30 ± 0.06%, a linear-shrinkage ratio of 0.71 ± 0.03%, a UCS of 1.856 ± 0.089 MPa, and an electrical resistivity of 297.55 ± 13.69 Ω·m. The 8–10 h groups therefore retained the highest mechanical, dimensional, and electrical performance within the investigated range.

(2) RML immersion produced a staged response rather than continuous strength loss. UCS and electrical resistivity generally increased during the first 7 d and subsequently stabilized or declined slightly, whereas mass loss and surface roughening developed gradually over 28 d. Because the RML and wetting–drying protocols imposed different hydraulic, thermal, and chemical actions, their results were interpreted independently rather than converted into a common severity ranking.

(3) Electrical resistivity changed consistently with UCS within each exposure regime and can serve as a comparative non-destructive indicator under the specified conditioning procedures. The combined SEM and XRD observations qualitatively support pore filling and improved cemented-skeleton continuity after carbonation, followed by local pore development, product debonding, dissolution, and reorganization during prolonged exposure.

(4) Carbonation and exposure reduced pH, but lower pH did not correspond directly to poorer mechanical durability. Under the adopted standardized extraction conditions, hazardous-element leaching remained below the comparison values, indicating that the carbonated backfill retained a low laboratory leaching response after both exposure regimes.

(5) At a UCS threshold of 0.8 MPa, the fitted models yielded wetting–drying strength-threshold exposures of 6.92–13.98 cycles and RML strength-threshold times of 45.69–75.05 d. The RML values extend beyond the 28 d measurement period and are therefore treated as model-based extrapolations for relative comparison rather than experimentally verified field service lives.

Future studies will compare deionized water and diluted red mud filtrate as wetting media and incorporate quantitative pore-structure characterization, quantitative phase analysis, and uncarbonated XRD reference specimens. The influence of specimen geometry will also be examined to improve the evaluation of coupled physical–chemical deterioration and the applicability of the laboratory results to field conditions.

https://doi.org/10.3390/buildings16153121

Supplementary Materials: The following supporting information can be downloaded at: https://www.mdpi.com/article/10.3390/buildings16153121/s1, Table S1: Mass and mass-loss ratio under wetting–drying cycles and RML immersion; Table S2: Specimen height and linear-shrinkage ratio under wetting–drying cycles and RML immersion; Table S3: Unconfined compressive strength under wetting–drying cycles and RML immersion; Table S4: Electrical resistivity under wetting–drying cycles and RML immersion; Table S5: pH under wetting–drying cycles and RML immersion.

Author Contributions: Conceptualization, L.Q. and X.D.; methodology, S.C. and J.Y.; formal analysis, T.Z.; writing—original draft, L.Q.; writing—review and editing, S.C., X.D. and J.Y.; visualization, D.C.; and supervision, S.C. and J.Y. All authors have read and agreed to the published version of the manuscript.

Funding: This work was supported by the National Natural Science Foundation of China (Grant No. 52378360), the Science and Technology Innovation Leading Talent Project of the Sanjin Talents Program (Grant No. SJYC2025012), and the Graduate Education Innovation Program of Shanxi Province (Grant No. 2025TD06).

Data Availability Statement: The corresponding author will provide the data generated or analysed during this study upon reasonable request.

Acknowledgments: The authors gratefully acknowledge the laboratory and technical support provided during sample preparation, mechanical testing, environmental testing, and microstructural characterization.

Conflicts of Interest: Author Junlian Yin was employed by the company Coal Industry Taiyuan Design and Research Institute Group Co., Ltd. The remaining authors declare that the research was conducted in the absence of any commercial or financial relationships that could be construed as a potential conflict of interest.

Abbreviations

Abbreviation	Definition
CFB	circulating fluidized bed
RML	red mud liquor
UCS	unconfined compressive strength
SEM	scanning electron microscopy
XRD	X-ray diffraction
M-S-H	magnesium silicate hydrate
M-A-S-H	magnesium aluminosilicate hydrate
C-A-S-H	calcium aluminosilicate hydrate
N-A-S-H	sodium aluminosilicate hydrate

References

1. Cui, W.; Dong, X.; Duan, W.; Liu, J.; Zhao, R.; He, G. Design of all solid waste red mud-based cementitious materials based on the simplex centroid method. *Constr. Build. Mater.* **2024**, *418*, 135439. [CrossRef]
2. Cui, W.; Cui, Q.; Dong, X.; Liu, J.; Song, K.; Xie, M.; Yao, X. Current research status and emerging trends in utilization of red mud resources: A study based on bibliometric network analysis. *Constr. Build. Mater.* **2024**, *442*, 137605. [CrossRef]
3. Liu, W.; Yang, J.; Xiao, B. Review on treatment and utilization of bauxite residues in China. *Int. J. Miner. Process.* **2009**, *93*, 220–231. [CrossRef]
4. Archambo, M.; Kawatra, S.K. Red mud: Fundamentals and new avenues for utilization. *Miner. Process. Extr. Metall. Rev.* **2021**, *42*, 427–450. [CrossRef]
5. Khairul, M.A.; Zanganeh, J.; Moghtaderi, B. The composition, recycling and utilisation of Bayer red mud. *Resour. Conserv. Recycl.* **2019**, *141*, 483–498. [CrossRef]
6. Liu, Y.; Lin, C.; Wu, Y. Characterization of red mud derived from a combined Bayer process and bauxite calcination method. *J. Hazard. Mater.* **2007**, *146*, 255–261. [CrossRef] [PubMed]
7. Zhang, W.; Liu, X.; Wang, Y.; Li, Z.; Li, Y.; Ren, Y. Binary reaction behaviors of red mud based cementitious material: Hydration characteristics and Na^+ utilization. *J. Hazard. Mater.* **2021**, *410*, 124592. [CrossRef] [PubMed]

8. Gong, C.; Yang, N. Effect of phosphate on the hydration of alkali-activated red mud–slag cementitious material. *Cem. Concr. Res.* **2000**, *30*, 1013–1016. [CrossRef]
9. Tang, W.C.; Wang, Z.; Liu, Y.; Cui, H.Z. Influence of red mud on fresh and hardened properties of self-compacting concrete. *Constr. Build. Mater.* **2018**, *178*, 288–300. [CrossRef]
10. Tang, W.C.; Wang, Z.; Donne, S.W.; Forghani, M.; Liu, Y. Influence of red mud on mechanical and durability performance of self-compacting concrete. *J. Hazard. Mater.* **2019**, *379*, 120802. [CrossRef] [PubMed]
11. Manfroi, E.P.; Cheriaf, M.; Rocha, J.C. Microstructure, mineralogy and environmental evaluation of cementitious composites produced with red mud waste. *Constr. Build. Mater.* **2014**, *67*, 29–36. [CrossRef]
12. Krivenko, P.; Kovalchuk, O.; Pasko, A.; Croymans, T.; Hult, M.; Lutter, G.; Vandevenne, N.; Schreurs, S.; Schroeyers, W. Development of alkali activated cements and concrete mixture design with high volumes of red mud. *Constr. Build. Mater.* **2017**, *151*, 819–826. [CrossRef]
13. Hairi, S.N.M.; Jameson, G.N.L.; Rogers, J.J.; MacKenzie, K.J.D. Synthesis and properties of inorganic polymers (geopolymers) derived from Bayer process residue (red mud) and bauxite. *J. Mater. Sci.* **2015**, *50*, 7713–7724. [CrossRef]
14. Bian, J.; Li, S.; Zhang, Q. Experimental investigation on red mud from the Bayer process for cemented paste backfill. *Int. J. Environ. Res. Public Health* **2022**, *19*, 11926. [CrossRef] [PubMed]
15. Wang, Z.; Wang, Y.; Wu, L.; Wu, A.; Ruan, Z.; Zhang, M.; Zhao, R. Effective reuse of red mud as supplementary material in cemented paste backfill: Durability and environmental impact. *Constr. Build. Mater.* **2022**, *328*, 127002. [CrossRef]
16. Li, S.; Zhang, R.; Feng, R.; Hu, B.; Wang, G.; Yu, H. Feasibility of recycling Bayer process red mud for the safety backfill mining of layered soft bauxite under coal seams. *Minerals* **2021**, *11*, 722. [CrossRef]
17. Wie, Y.M.; Lee, K.G.; Lee, K.H. Characteristics of circulating fluidized bed combustion (CFBC) ash as carbon dioxide storage medium and development of construction materials by recycling carbonated ash. *Materials* **2024**, *17*, 4359. [CrossRef] [PubMed]
18. Jia, G.; Wang, Y.; Yang, F. A review on the application of circulating fluidized bed fly ash in building materials. *Adv. Mater. Sci. Eng.* **2022**, *2022*, 7099430. [CrossRef]
19. Chi, M. Synthesis and characterization of mortars with circulating fluidized bed combustion fly ash and ground granulated blast-furnace slag. *Constr. Build. Mater.* **2016**, *123*, 565–573. [CrossRef]
20. Jang, J.G.; Park, S.M.; Chung, S.; Ahn, J.W.; Kim, H.K. Utilization of circulating fluidized bed combustion ash in producing controlled low-strength materials with cement or sodium carbonate as activator. *Constr. Build. Mater.* **2018**, *159*, 642–651. [CrossRef]
21. Zhang, W.; Choi, H.; Sagawa, T.; Hama, Y. Compressive strength development and durability of an environmental load-reduction material manufactured using circulating fluidized bed ash and blast-furnace slag. *Constr. Build. Mater.* **2017**, *146*, 102–113. [CrossRef]
22. Wu, R.; Dai, S.; Jian, S.; Huang, J.; Lv, Y.; Li, B.; Nurmirzayev, A. Utilization of the circulating fluidized bed combustion ash in autoclaved aerated concrete: Effect of superplasticizer. *Constr. Build. Mater.* **2020**, *237*, 117644. [CrossRef]
23. Zahedi, M.; Jafari, K.; Rajabipour, F. Properties and durability of concrete containing fluidized bed combustion (FBC) fly ash. *Constr. Build. Mater.* **2020**, *258*, 119663. [CrossRef]
24. Mo, L.; Zhang, F.; Panesar, D.K.; Deng, M. Development of low-carbon cementitious materials via carbonating Portland cement–fly ash–magnesia blends under various curing scenarios: A comparative study. *J. Clean. Prod.* **2017**, *163*, 252–261. [CrossRef]
25. Pu, L.; Unluer, C. Durability of carbonated MgO concrete containing fly ash and ground granulated blast-furnace slag. *Constr. Build. Mater.* **2018**, *192*, 403–415. [CrossRef]
26. Unluer, C.; Al-Tabbaa, A. Impact of hydrated magnesium carbonate additives on the carbonation of reactive MgO cements. *Cem. Concr. Res.* **2013**, *54*, 87–97. [CrossRef]
27. Ruan, S.; Unluer, C. Influence of mix design on the carbonation, mechanical properties and microstructure of reactive MgO cement-based concrete. *Cem. Concr. Compos.* **2017**, *80*, 104–114. [CrossRef]
28. Wang, L.; Chen, L.; Provis, J.L.; Tsang, D.C.W.; Poon, C.S. Accelerated carbonation of reactive MgO and Portland cement blends under flowing CO_2 gas. *Cem. Concr. Compos.* **2020**, *106*, 103489. [CrossRef]
29. Dung, N.T.; Unluer, C. Carbonated MgO concrete with improved performance: The influence of temperature and hydration agent on hydration, carbonation and strength gain. *Cem. Concr. Compos.* **2017**, *82*, 152–164. [CrossRef]
30. Dung, N.T.; Unluer, C. Development of MgO concrete with enhanced hydration and carbonation mechanisms. *Cem. Concr. Res.* **2018**, *103*, 160–169. [CrossRef]
31. Hay, R.; Celik, K. Hydration, carbonation, strength development and corrosion resistance of reactive MgO cement-based composites. *Cem. Concr. Res.* **2020**, *128*, 105941. [CrossRef]
32. Dung, N.T.; Lesimple, A.; Hay, R.; Celik, K.; Unluer, C. Formation of carbonate phases and their effect on the performance of reactive MgO cement formulations. *Cem. Concr. Res.* **2019**, *125*, 105894. [CrossRef]
33. Kuenzel, C.; Zhang, F.; Ferrandiz-Mas, V.; Cheeseman, C.R.; Gartner, E.M. The mechanism of hydration of MgO–hydromagnesite blends. *Cem. Concr. Res.* **2018**, *103*, 123–129. [CrossRef]
34. Soares, E.G.; Castro-Gomes, J. Carbonation curing influencing factors of carbonated reactive magnesia cements (CRMC): A review. *J. Clean. Prod.* **2021**, *305*, 127210. [CrossRef]

35. Wang, D.; Zhu, J.; He, F. Quantification and micro-mechanisms of CO_2 sequestration in magnesia–lime–fly ash/slag solidified soils. *Int. J. Greenh. Gas. Control* **2019**, *91*, 102827. [CrossRef]
36. Bonenfant, D.; Kharoune, L.; Sauvé, S.; Hausler, R.; Niquette, P.; Mimeault, M.; Kharoune, M. CO_2 sequestration by aqueous red mud carbonation at ambient pressure and temperature. *Ind. Eng. Chem. Res.* **2008**, *47*, 7617–7622. [CrossRef]
37. Chen, Q.Y.; Tyrer, M.; Hills, C.D.; Yang, X.M.; Carey, P. Immobilisation of heavy metal in cement-based solidification/stabilisation: A review. *Waste Manag.* **2009**, *29*, 390–403. [CrossRef] [PubMed]
38. Li, S.; Zhang, Y.; Feng, R.; Yu, H.; Pan, J.; Bian, J. Environmental safety analysis of red mud-based cemented backfill on groundwater. *Int. J. Environ. Res. Public Health* **2021**, *18*, 8094. [CrossRef] [PubMed]
39. Shi, Y.; Zhang, Z.; Sang, Z.; Zhao, Q. Microstructure and composition of red mud–fly ash-based geopolymers incorporating carbide slag. *Front. Mater.* **2020**, *7*, 563233. [CrossRef]
40. Long, Q.; Zhao, Y.; Zhang, B.; Yang, H.; Luo, Z.; Li, Z.; Zhang, G.; Liu, K. Interfacial behavior of slag, fly ash, and red mud-based geopolymer mortar with concrete substrate: Mechanical properties and microstructure. *Buildings* **2024**, *14*, 652. [CrossRef]
41. Wang, X.; Xue, Y. Preparation and immobilization mechanism of red mud/steel slag-based geopolymers for solidifying/stabilizing Pb-contaminated soil. *Materials* **2024**, *17*, 3353. [CrossRef] [PubMed]
42. Occhicone, A.; Vukčević, M.; Bošković, I.; Mingione, S.; Ferone, C. Alkali-activated red mud and construction and demolition waste-based components: Characterization and environmental assessment. *Materials* **2022**, *15*, 1617. [CrossRef] [PubMed]
43. Qian, L.-P.; Ahmad, M.R.; Lao, J.-C.; Dai, J.-G. Recycling of red mud and flue gas residues in geopolymer aggregates (GPA) for sustainable concrete. *Resour. Conserv. Recycl.* **2023**, *191*, 106893. [CrossRef]
44. Hu, W.; Li, K.; Yin, W.; Zhang, H.; Xue, Y.; Han, Y.; Liu, P. Effects of wetting–drying cycles on the macro and micro properties of the cement-stabilized soil with curing agent. *Buildings* **2024**, *14*, 1716. [CrossRef]

Disclaimer/Publisher's Note: The statements, opinions and data contained in all publications are solely those of the individual author(s) and contributor(s) and not of MDPI and/or the editor(s). MDPI and/or the editor(s) disclaim responsibility for any injury to people or property resulting from any ideas, methods, instructions or products referred to in the content.